Arabian Journal of Chemistry (2021) **14**, 103121

King Saud University

Arabian Journal of Chemistry

www.ksu.edu.sa
www.sciencedirect.com

ORIGINAL ARTICLE

Self-assembled oil palm biomass-derived modified graphene oxide anode: An efficient medium for energy transportation and bioremediating Cd (II) via microbial fuel cells

Asim Ali Yaqoob [a], **Albert Serrà** [b,c], **Mohamad Nasir Mohamad Ibrahim** [a,*], **Amira Suriaty Yaakop** [d]

[a] *Materials Technology Research Group (MaTRec), School of Chemical Sciences, Universiti Sains Malaysia, 11800 Minden, Penang, Malaysia*
[b] *Thin Films and Nanostructures Electrodeposition Group (GE-CPN), Department of Materials Science and Physical Chemistry, University of Barcelona, Martí i Franquès 1, E-08028 Barcelona, Catalonia, Spain*
[c] *Institute of Nanoscience and Nanotechnology (IN^{2}UB), University of Barcelona, E-08028 Barcelona, Catalonia, Spain*
[d] *School of Biological Sciences, Universiti Sains Malaysia, 11800 Minden, Penang, Malaysia*

Received 12 February 2021; accepted 9 March 2021
Available online 24 March 2021

KEYWORDS

Microbial fuel cell;
Anode modification;
Graphene oxide anode;
Wastewater treatment;
Energy generation

Abstract Although microbial fuel cells (MFCs) rank among the most promising bioelectrochemical approaches for generating energy while removing pollutants from wastewater, their relatively poor performance, largely due to electrode material that hinder their applicability, has limited their commercial viability. Thus, in our study, self-assembled modified graphene oxide (GO) anodes were developed from oil palm (Elaeis guineensis) biomass, and several techniques were applied to assess the physiochemical properties of material synthesized with waste material. Ultimately, the waste material was an excellent source for generating energy in the form of anodes in MFCs. The bioinspired modified GO anodes demonstrated greater energy output (135.96 mA/m^2) of more than eight times the unmodified GO anodes (15.65 mA/m^2), even though the source of inoculation was synthetic wastewater with 100 ppm of Cd (II) solution. To our knowledge, no work has reported removing Cd (II) from synthetic wastewater by using waste-derived anodes via MFCs. This paper reports on the utilization of waste-derived organic waste (oil palm trunk sap) as an organic sub-

* Corresponding author.
E-mail address: mnm@usm.my (M.N.M. Ibrahim).
Peer review under responsibility of King Saud University.

Production and hosting by Elsevier

https://doi.org/10.1016/j.arabjc.2021.103121

strate which is a healthy source of nutrients for bacteria in an inoculated media. Along with evidence of their electrochemical and biological character, the primary result achieved (i.e., 90% removal efficiency) supports using MFCs on an industrial scale.

1. Introduction

Two of today's most alarming environmental issues—heavy metal pollution and an energy crisis—stand at the crux of wastewater treatment. Despite several types of biological, chemical, and physical approaches to treating metal pollution in wastewater resources, they all pose various drawbacks, including high energy requirements as well as high operating costs, the intensive consumption of chemicals, and the production of waste as a by-product (Yaqoob et al., 2020a). Among those disadvantages, the high amount of energy needed to treat wastewater coincides with a worldwide energy crisis due to diverse environmental changes currently transforming the planet. In response, immense effort has been devoted to developing a cost-effective, low-energy method of removing toxic metals from wastewater (Vardhan et al., 2019).

Owing to their sustainability and low cost, microbial fuel cells (MFCs) have been recognized as a viable technology for producing energy and removing toxic metals from wastewater resources. Along with a proton exchange membrane (PEM), MFCs consist of two electrodes—an anode and a cathode—the former of which is responsible for providing sufficient space for bacterial growth and extracellular electron transfer in order to oxidize organic matter in wastewater and thereby generate protons and electrons. Although that approach has received sustained attention for its capacity to generate renewable energy and treat wastewater, MFCs have lacked commercial viability due to their low efficiency (Logan and Rabaey, 2012; Yaqoob et al., 2020b).

Several parameters directly affect the performance of MFCs: their scaling and design, the PEM's efficiency, cell resistance, the organic substrate, and the materials used for the electrodes, to name a few. Of those parameters, the material of the anode critically affects the performance of MFCs by facilitating bacterial species adhesion on the material's surface and, in turn, improving the transferability of electrons (Kannan, 2016). To date, several types of electrode materials have been investigated, including carbon (e.g., cloth, rod, sheet, foam, carbon nanotubes, and sponges), graphite (e.g., rod, sheet, and cloth), metal-based electrodes, and graphene-derived electrodes. Although all of those materials also have drawbacks—high cost, limited conductivity, and limited biocompatibility— among the carbon allotropes graphene derivatives have demonstrated excellent properties, including large surface area, high electron mobility, robust mechanical strength, high thermal stability, and good chemical stability with reasonable electrical conductivity (Yaqoob et al., 2020c). Moreover, by minimizing limitations such as their electrical conductivity and the cost of graphene derivatives, graphene-derived electrodes can become usable on a commercial scale. Considering all of the above, composite-based electrodes may enhance the performance of anodes, improve the electrical conductivity of MFCs, and thus make their industrial-scale use viable. Whereas metal-based materials also demonstrate properties beneficial to anodes, their corrodibility curtails the performance of their anodes (Pareek et al., 2019).

Therefore, a graphene–metal oxide composite seemed to be a novel, bioinspired material suitable for the task, added to the fact that graphene's cost can be reduced by using waste material to prepare graphene oxide (GO). Indeed, that process has also recently attracted considerable attention in various fields. Thus far, several waste materials have been used in electrodes, including compressed milling residue, loofah sponges, coconut shells, corn straw, mushrooms, silk cocoons, onion peels, cocklebur fruit, and even pinecones (Karthikeyan et al., 2015; Wang et al., 2019; Yang et al., 2019; Yaqoob et al., 2020d).

In our study, the proposed bioinspired material drew upon the synthesis of GO from lignin produced by various plants in Malaysia, a country rich in oil palm resources and industries dedicated to their application. In an exceptionally cost-effective process, lignin can be converted into GO via simple carbonization and Hummers's method, after which the composite of lignin-based GO (L-GO) and ZnO can serve as the anode material. ZnO is highly conductive and inexpensive. Recently, Shakeel et al. (2020) reported the introduction of the ZnO with polyindole functionalized multi-walled CNTs and used as an anode electrode in enzymatic biofuel cells. They concluded that the introduction of ZnO increased the electrochemical performance and the achieved maximum current density was 4.9 mA/cm^2. Therefore, the introduction of ZnO as a modifier in GO can be useful to improve the electron transport rate and electrocatalytic activities. In this article, we compare the performance of the anode materials L-GO and L-GO–ZnO in the removal of cadmium, Cd (II), from synthetic wastewater toxic to humans. Additionally, the detailed explanation of the MFCs mechanism (anode oxidation) and comparative profile was discussed briefly.

2. Experimental section

2.1. Materials

Palm oil waste (Sabutek (M) Sdn. Bhd), sodium nitrate (Sigma-Aldrich), potassium permanganate (Sigma-Aldrich), hydrochloric acid (AR), hydrogen peroxide (30–32%, QRëC), dichloromethane (QRëC), sulfuric acid (95–97%, QRëC), ethanol (approx. 95%, QRëC), polysulfones (M_w = approx. 35,000, Sigma-Aldrich), polylactic acid (M_w = approx. 60,000, Sigma-Aldrich), 70-mm filter paper (Advantec), cadmium nitrate tetrahydrate (ACROS), zinc oxide (chemPUR), deionized (DI) water, pond wastewater from Universiti Sains Malaysia, and oil palm trunk sap donated by Dr. Rokiah Hashim's research group in the School of Industrial Technology at Universiti Sains Malaysia.

2.2. Preparation of lignin and carbonized carbon from palm oil waste

Lignin was prepared by acidification. First, 250 g of oil palm empty fruit bunch was treated with 30% NaOH solution in a pulping machine, 3 L of water was added, and the pulping machine was operated continuously for 180 min at 175 ℃. The materials obtained were black liquor, which served as raw material for lignin, and solid waste known as cellulose, which is mostly used in the paper industry. The black liquor was separated from the solid waste by squeezing and further treated for the extraction of lignin. Last, the black liquor was centrifuged 8 times for 15 min at 4000 rpm to decontaminate the lignin liquid and dried at 45 °C. To reduce the effect of moisture on the dried lignin powder, the extracted sample was pulverized into a fine powder and heated at 40 °C for more than 24 h (Sekeri et al., 2020). The extracted lignin powder was used to convert the fine powder into carbonized carbon by sim-

ple carbonization, which caused the synthesis of GO. The dried lignin was baked at 1,100 ℃ in a furnace in the presence of an argon flow running at 15 ℃/min. The furnace parameters were maintained for 180 min prior to annealing, for which the furnace temperature was reduced to 40 ℃. The carbonized flakes obtained as a result were further pulverized in a grinding machine to obtain a fine carbonized powder known as L-carbon.

2.3. Synthesis of L-GO and L-GO–ZnO composite

The L-carbon was used to synthesize GO in the form of lignin derived graphene oxide (L-GO) (Zaaba et al., 2017). In that process, L-carbon (5 g) and $NaNO_3$ (7 g) were treated continuously for 90 min in the presence of H_2SO_4 (150 mL) under magnetic stirring. After 90 min, $KMnO_4$ (15 g) was added at 0–5 °C under constant stirring for at least 180 min in an ice bath. When the sample was removed from the ice bath and kept for 30 h for proper oxidation, its color changed from black to violet brown. DI (150 mL) was added dropwise into the solution and the reaction stirred at 90 °C until a dark brown solution was obtained, at which point the reaction was removed from heat and cooled until reaching room temperature. At room temperature, 200 mL of water and H_2O_2 (30%) was added to complete the reaction and remove the effect of $KMnO_4$. The obtained liquid GO sample was washed with ethanol and DI water several times and dried to obtain the L-GO powder.

To modify the properties of L-GO to create a novel electrode, a composite with zinc oxide (ZnO; Sigma Aldrich) was prepared, namely the L-GO–ZnO composite, via the relatively easy solvothermal method. After 5 g of synthesized L-GO was mixed with commercial ZnO (2.5 g) in the presence of ethanol (150 mL) under constant stirring for 3 h at room temperature, the sample was washed with DI water and ethanol, dried at 150 °C for 12 h, and vigorously pulverized to obtain a fine L-GO–ZnO composite powder.

2.4. Fabrication of anodes

The prepared L-GO and L-GO–ZnO were used to fabricate two types of anode electrodes for MFCs: The L-GO-based anode and L-GO–ZnO-based anode. A 2-mm graphite rod was utilized as a current collector and supportive material, while polysulfones served as a binding material in the fabrication process. First, 3 g of L-GO was vigorously mixed with a homogeneous mixture of polysulfones to obtain a paste to coat the surface of the current collector, dried at 35 °C for 12 h. After proper heating, the prepared cylindrical rod-shaped electrode was ready for use as an anode. Second, 3 g of L-GO–ZnO composite paste with polysulfones (2 g) was used to coat the current collector and thereby produce the L-GO–ZnO composite electrode. The size (8.0 cm height and 1.3 cm radius, and the calculated surface area was 76.0 cm^2) and composition of both electrodes were identical.

2.5. Characterization of anode-based materials

The morphology and physical properties of the L-GO and L-GO–ZnO composite prepared for anode fabrication were characterized by using several techniques. Whereas Fourier-transform infrared (FT-IR; Perkin Elmer model System 2000; Norwalk, CT, USA) and UV spectroscopy (UV-2600i Shimadzu UV–VIS; Kyoto, Japan), Raman spectroscopy (RA-82; Renishaw inVia Raman microscope, USA), transmission electron microscopy (TEM; Model Zeiss Libra 120; Jena, Germany), energy-dispersive X-ray (EDX; Quanta FEG 650, Fei; Columbia, MO, USA), and scanning electron microscopy (SEM-Quanta FEG 650, Fei; Columbia, MO, USA) were used to evaluate the functional groups and physical properties of the products, thermal gravimetric analysis (TGA-Perkin Elmer Thermal Analyser, model TGA/SDTA 851; Akron, OH, USA), atomic force microscopy (AFM; SII Sciko Instrument INC SPI 3800 N Probe station; New York, NY, USA) and the Brunauer–Emmett–Teller (BET; V-Sorb 4800S Brunauer, Beijing; China) method were used to determine the thermal stability, surface roughness, and surface area. By contrast, the crystalline structure was observed with X-ray diffraction (XRD; Philips PW 1710 X-ray diffractometer; New York, NY, USA). The chemical analysis was done by using X-ray photoelectron spectroscopy (XPS; Axis Ultra DLD XPS, Kratos; Manchester, M17, UK).

2.6. Microbial fuel cells: Setup and operational mode

The experiment was conducted by using double-chamber MFCs (DMFCs), consisting of anode and cathode chambers separated by a PEM (Nafion 117), and the fabricated L-GO and L-GO–ZnO composite anode electrodes. The design of the MFCs and the fabricated anodes appears in Fig. 1. The size of the anode and cathode chambers of the DMFCs was 10 × 9.5 cm and 10 × 9 cm, respectively, and each was 1 L in volume. The local wastewater was collected from a pond at Universiti Sains Malaysia and supplemented with Cd (II) solution (100 ppm). Cd (II) supplemented wastewater was known as synthetic wastewater in the present study and was used as an inoculation source in the operation. The addition of Cd (II) was carried out to evaluate the anode performance in term of removal efficiency. The physiochemical properties of raw and synthetic wastewater are shown in Table 1. Further, Nafion-117 was again used as a PEM to pass the protons from the anode to the cathode chamber, for which the PEM was treated before use with DMFCs as advised by Liu and Logan (2004). The L-GO and L-GO–ZnO composite anode electrodes were separately used in DMFC reactors with a graphite rod (2B pencil lead, Fuda) as a cathode. The cathode electrode's size (8 × 1.3 cm) and space between the anode and cathode in each reactor (7 cm) was identical. An external resistance of 1000 Ω, achieved by connecting Cu wires in both reactors, was used; however, in operational mode, the glucose with fresh pond water solution (2.5 g/L) was used every day to minimize the evaporation of water. The oil palm trunk sap, a healthy source nutrient for bacteria in an inoculated media, was used as an organic substrate. To maintain the aerobic environment, external oxygen was supplied to each reactor, in which the cathode chamber was filled with surface water containing several types of electrolytes. The pH of the cathode surface water was 7.0. The entire operation was performed at room temperature. Both anode operations were conducted in duplicate to verify the efficiency of both electrodes in synthetic wastewater through MFCs. Additionally, the thermometer (GH, Zeal Ltd. China), electrical meter (ECM; Alpha-800

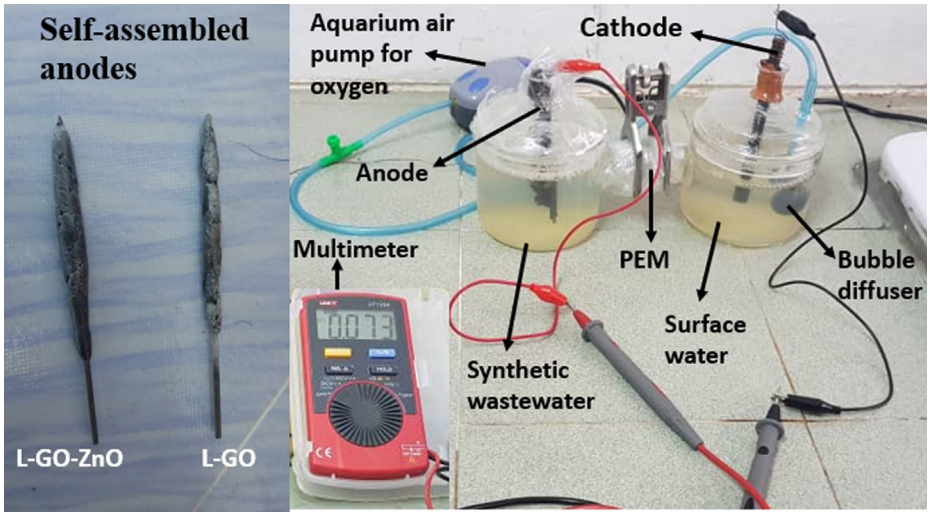

Fig. 1 Operating MFC system with fabricated L-GO and L-GO–ZnO composite anode electrodes.

Table 1 The physiochemical properties of local collected wastewater and supplemented wastewater.

Physicochemical analysis	Raw wastewater	Metal supplemented wastewater
Colour	Light yellowish	Light yellowish
Electrical conductivity	70 μS/cm	81 μS/cm
Temperature	25 ± 1 °C	25 ± 1 °C
Odor	Unpleasant	Unpleasant
pH	6.94	6.41
Cd (II)	0 ppm	100 ppm

conductivity meter, China), and pH meter (EUTECH instrument-700 USA), were used to analyze the physiochemical properties.

2.7. Electrochemical analysis of MFCs

Different electrochemical tests were performed to evaluate the efficiency of the power density (PD) and current density (CD) produced in results of the novel anode electrodes. The polarization behavior and PD curves were analyzed by raising the external resistance from 150 Ω to 10 kΩ when the voltage potential indicated a constant output. Voltage was determined by using a digital multimeter (UNI-T, Model UT120A, China), and Eqs. (1) and (2) were used to calculate PD and CD from the observed voltage:

$$(\mathrm{PD}) = \frac{\mathrm{V}^{2}}{\mathrm{RA}} \tag{1}$$

$$(\mathrm{J}) = \frac{\mathrm{I}}{\mathrm{A}} \tag{2}$$

in which V is voltage, R is resistance, A is surface area, and J is CD.

To examine the redox reaction of the cells, cyclic voltammetry (CV; Model BAS Epsilon Version 1.4; West Lafayette, IN, USA) was applied by using a potentiostate system on Days 20, 40, 60, and 80 to evaluate the microbial community's bioelectrochemical performance on the surface of the anodes. The scan rate was 20 mV/s within the potential range (+0.8 to −0.8 V). A Pt wire served as a counter-electrode, whereas a glassy carbon electrode served as the working electrode and Ag–AgCl worked as the reference electrode. Data from CV can also help to calculate specific capacitance (C_s)—that is, the integration over the entire set of statistics per unit area of electrode. Eq. (3) was used to determine C_s on the mentioned days:

$$\mathrm{Cs} = \frac{\mathrm{A}}{2\mathrm{mk}(\mathrm{V2} - \mathrm{V1})} \tag{3}$$

In which A is the CV's curve area, m is the loaded quantity of the sample, k is the scan rate (mV/s), and $\Delta V = (V2 - V1)$ is the CV's potential range (i.e., total voltage range). At the same time, electrochemical impedance spectroscopy (EIS; Gamry Reference 600; Warminster, PA, USA) was used to study the resistance effect of electrodes from the electrolyte solution. Measurement with EIS was performed on Day 80 of the operation of the MFCs in order to study their electrochemical parameters in the frequency range of 100 kHz to 100 mHz. To avoid the detachment of the biofilm, the steady AC amplitude was 1 mV. Each spectrum required approximately 15–20 min until completion with a scene range of 0.5–0.1 Hz.

2.8. Removal efficiency and bacterial community analysis

The removal efficiency of Cd (II) was observed every 10 days, when a 1.5-mL sample was collected from the anode cells and analyzed with atomic adsorption spectrometer (PerkinElmer A Analyst 400; Waltham, MA, USA). Eq. (4) is used to calculate the removal efficiency:

$$\mathrm{RE}\% = \frac{TM\mathrm{initial} - TM\mathrm{final}}{TM\mathrm{initial}} \times 100 \tag{4}$$

in which RE% is removal efficiency, $TM_{initial}$ is the initial toxic metal concentration, and TM_{final} is the final toxic concentration of the metal. In addition, SEM and EDX (DSM-960, Carl Zeiss) were used to study the biofilm's morphology present on both anode electrodes (i.e., L-GO and L-GO–ZnO composite).

The EDX of the treated anodes was performed to analyze the biocompatibility of the fabricated anodes in a highly toxic solution—that is, Cd (II)—and to confirm the non-adsorption of Cd (II) on the surface of the fabricated anodes. Prior to SEM, the electrode was carefully washed with natural buffer solution and glutaraldehyde solution. SEM was performed without any coating on the L-GO and L-GO–ZnO anodes.

To identify the bacteria species in the cells, the biofilm produced (1 mm) was scratched from the surface of the L-GO and L-GO–ZnO anodes and kept in distilled water. Serial dilution was used to transfer the colonies onto nutrient agar plates, and once the plates revealed different colonies requiring further purification, each colony was carefully purified to identify bacterial species. The bacterial 16S rRNA genes were obtained by polymerase chain reaction (PCR), with a forward primer (27F) and reverse primer (1492R) used to amplify the product. A cloning kit (TOPO TA, Carlsbad, Invitrogen, USA) was used to clone the PCR-amplified product, and after DNA sequencing, 16S rRNA bacterial strains were deposited in GenBank.

3. Results and discussion

3.1. Characterization of prepared electrodes

When explored with FTIR spectroscopy, the formation of the L-GO–ZnO composite (Fig. 2**a**) clearly revealed L-GO's representative oxygen-containing functional groups, ascribed to C—OH stretching vibrations, C—O—H deformation, C—O stretching vibrations, and the C═O stretching of COOH groups by peaks at approximately 1236, 1401, 1074, and 1728 cm^{-1}, respectively. Bands at 1050 cm^{-1}, attributed to the C—O stretching vibrations mixed with C—OH bending, and at 1603 cm^{-1}, associated with the C═C skeletal vibrations of L-GO, were also easily observed. In addition, a broad peak that emerged at approximately 3250 cm^{-1} seemed to correspond to the hydroxyl stretching vibrations of the C—OH groups (Durmus et al., 2019). Those results are consistent with findings reported in the literature, which has shown that the presence of such oxygen-containing functional groups significantly increases GO's hydrophilic properties and interlayer spacing. The attachment of ZnO nanoparticles to L-GO after solvothermal treatment was confirmed by the appearance of another strong peak at approximately 460 cm^{-1}, attributable to the characteristic stretching vibration modes of Zn—O (Anandhavelu and Thambidurai, 2013).

Beyond that, the synthesized nanocomposite's crystalline behavior revealed by XRD analysis (Fig. 2**b**) confirmed L-GO's synthesis owing to a sharp peak at $2\theta = 10.2°$. That peak perfectly aligned with L-GO's (001) reflection and a broad diffraction peak at $2\theta = 24.2°$, which itself indicated GO's partial reduction. At the same time, the XRD pattern of the L-GO–ZnO composite was consistent with the ZnO hexagonal wurtzite structure (JCPDS no. 36-1451) (Li et al., 2013). Among other results, the strongest peaks observed at 2θ values of 31.79°, 34.421°, 36.252°, 47.51°, 56.602°, 62.862°, 67.961°, and 69.0° corresponded to the lattice planes (100), (002), (101), (110), (103), (112), and (201),

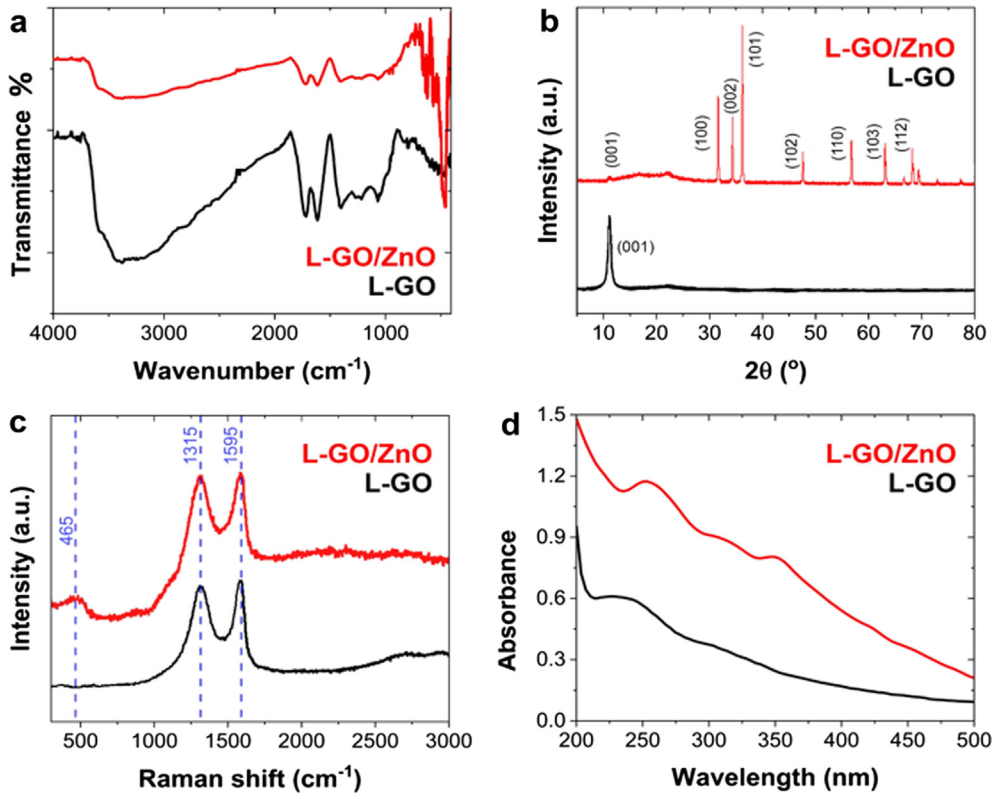

Fig. 2 (a) FTIR spectra, (b) XRD patterns, (c) Raman spectra, and (d) UV–vis absorption spectra of L-GO and the L-GO–ZnO composite.

respectively, as consistent with findings reported in the literature. XRD analysis additionally confirmed that ZnO nanoparticles were effectively anchored into the L-GO sheets. Further verifying the formation of L-GO and the L-GO–ZnO composite, Raman spectra (Fig. 2**c**) for the L-GO sample revealed two bands. On the one hand, the D band at 1,315 cm^{-1} emerged in response to the in-plane stretching motion of symmetric sp^2 C—C bonds and indicated L-GO's structural disorder; on the other, the G band at 1,595 cm^{-1} corresponded to an E_{2g} mode of hexagonal graphite and the vibration of the sp^2-hybridized carbon domain. As for the L-GO–ZnO composite, another band was observed at 465 cm^{-1}, which corresponded to the high E^2 mode of ZnO vibrations (Xu et al., 2015). Importantly, the intensity ratio of the D-to-G band (I_D/I_G) increases in the L-GO–ZnO composite (I_D/I_G = 0.96) compared to that of L-GO (I_D/I_G = 0.90). This increase in the I_D/I_G, approximately 6.7%, is attributed to the composite formation of L-GO and ZnO nanoparticles (Yang et al., 2019). That outcome confirmed the L-GO–ZnO nanohybrid's formation and endorsed the purity of the samples inferred from the FTIR spectra and XRD diffractogram.

When the optoelectronic properties of L-GO and the L-GO–ZnO composite were investigated via UV–vis spectroscopy (Fig. 2**d**), L-GO's spectra exhibited an absorption peak centered at approximately 235 nm and a shoulder at approximately 302 nm, which respectively corresponded to the ä→ä* transition of aromatic C–C bonds and the n→ä* transitions of C═O bonds. The spectra of the nanocomposites also exhibited another absorption peak at approximately 355 nm, which seemed to correspond to the absorption of ZnO nanoparticles (Umar et al., 2015). The peak and shoulder corresponding to L-GO were shifted at 255 and 305 nm, and the surface attachment of ZnO nanoparticles resulted in rapid electron transfer and increased transition energy. The bandgap energies calculated for L-GO and L-GO–ZnO were 5.1 and 3.35 eV, respectively, with the lower bandgap of the L-GO–ZnO composite expected to facilitate better conductivity (Chauhan et al., 2019).

To further investigate the chemical states of the elements of the prepared electrodes and the interaction between L-GO and ZnO nanoparticles in the composite electrode, the results of X-ray photoelectron spectroscopy were analyzed (Fig. 3). The deconvoluted high-resolution C 1s spectrum of L-GO revealed three peaks corresponding to C—C (284.6 eV), C—O (286.4 eV), and C═C (288.3 eV) functional groups, respectively (Al-Gaashani et al., 2019). After the solvothermal method was applied to incorporate ZnO nanoparticles, the intensity of C 1s peak reduced significantly, while the relative intensity of the deconvoluted peaks changed. An exceptionally clear shift appeared for the C—O and C═O bonds in the composite material, possibly due to the strong interaction between the oxygen functional groups of the L-GO and ZnO nanoparticles. After deconvolution, the O1s spectra of L-GO showed four peaks corresponding to O—C═O (530.9 eV), C═O (531.8 eV), C—OH (532.6 eV), and C—O—C (533.2 eV). However, after the ZnO nanoparticles were incorporated, the O 1s spectra of the L-GO–ZnO composite clearly showed three peaks, located at 529.9, 532.1, and 533.4 eV, which respectively corresponded to the O^{2-} ions in the ZnO hexagonal wurtzite structure, the oxygen vacancies in the matrix of ZnO, and the presence of chemical-adsorbed hydroxyls or oxygen on the electrode's surface. A Zn 2p signal was not detected in the case of L-GO, although two peaks at 1044.8 and 1021.5 eV corresponded to zinc $2p_{1/2}$ and $2p_{3/2}$, respectively, indicating the normal state of Zn^{2+} in the ZnO nanoparticles. No shift in the peak position of zinc 2p was observed, however, which indicates no C–Zn bond formation in the nanocomposite (Li et al., 2015). X-ray photoelectron spectra also confirmed the formation of L-GO and L-GO–ZnO electrodes.

The specific surface areas of the L-GO and L-GO–ZnO electrodes were also deemed critical to determining the efficiency of the electrodes, because large, accessible areas allow bacterial colonies to work more efficiently and facilitate the reduction of pollutants in MFCs. To examine their areas as well as their pore size and pore volume, the Brunauer–Emmett–Teller method from nitrogen adsorption–desorption isotherms was used (Kirubaharan et al., 2015). As shown in Table 2, the L-GO electrode exhibited a significantly larger surface area than L-GO–ZnO. Of course, several operational factors—conductivity, bacterial adhesion, and bacterial colonies—are also critical to determining the global performance of MFCs.

After the principal physiochemical properties of the L-GO and L-GO–ZnO electrodes were analyzed, the morphological and textural characteristics of each material were analyzed as well. First, FE-SEM and TEM were employed to observe the morphologies of the prepared anodes (Fig. 4**a–d**). As shown in Fig. 4**a and b**, L-GO exhibited an uncomplicated shape due to exfoliation, with irregular particles ranging from 10 to 85 nm. Similarly, the L-GO–ZnO composite showed irregular particles and aggregates ranging from 100 to 200 nm, while ZnO nanoparticles were approximately 100 nm. Beyond that, the elemental composition analysis of the results of EDX (**Fig. S1**) confirmed the high purity of synthesized L-GO, and the formation of L-GO–ZnO was compositionally confirmed by the 39% carbon content and 29% Zn (II) content detected in the composite material. Atomic force microscopy of the L-GO and L-GO–ZnO electrodes (**Fig. S2**) was additionally performed to further analyze characteristics of surface morphology, including roughness and uniformity. Both the L-GO and L-GO–ZnO electrodes exhibited smooth surfaces, which promotes the growth of bacteria. Additionally, Pt was detected in the EDX spectrum due to the coating of the sample.

3.2. Electrochemical study of MFCs

3.2.1. Energy generation and polarization behavior

When the electricity-generating capacity of the MFCs using the L-GO and L-GO–ZnO anodes was investigated during an operational period of 80 days (Fig. 5**a**), both anodes revealed a similar electricity-generating ability, especially initially, despite a considerable difference in the maximum stable voltage achieved. On Day 25, the L-GO anode demonstrated the greatest generation of electricity, at 111 ± 3 mV, with a PD and CD at Point 1 of 16.872 × 10^{-4} mW/m^2 and 14.605 mA/m^2, respectively, compared with 191 ± 4 mV achieved by the L-GO–ZnO anode. Thus, Points 1 and 4 seemed to exhibit the highest voltage stability with an external resistance of 1 kΩ, whereas using less than 1 kΩ of external resistance achieved less stability in generating electric current. After the third cycle, both electrodes, at Points 3 and 6, showed sharp declines in voltage beginning on Day 72 until

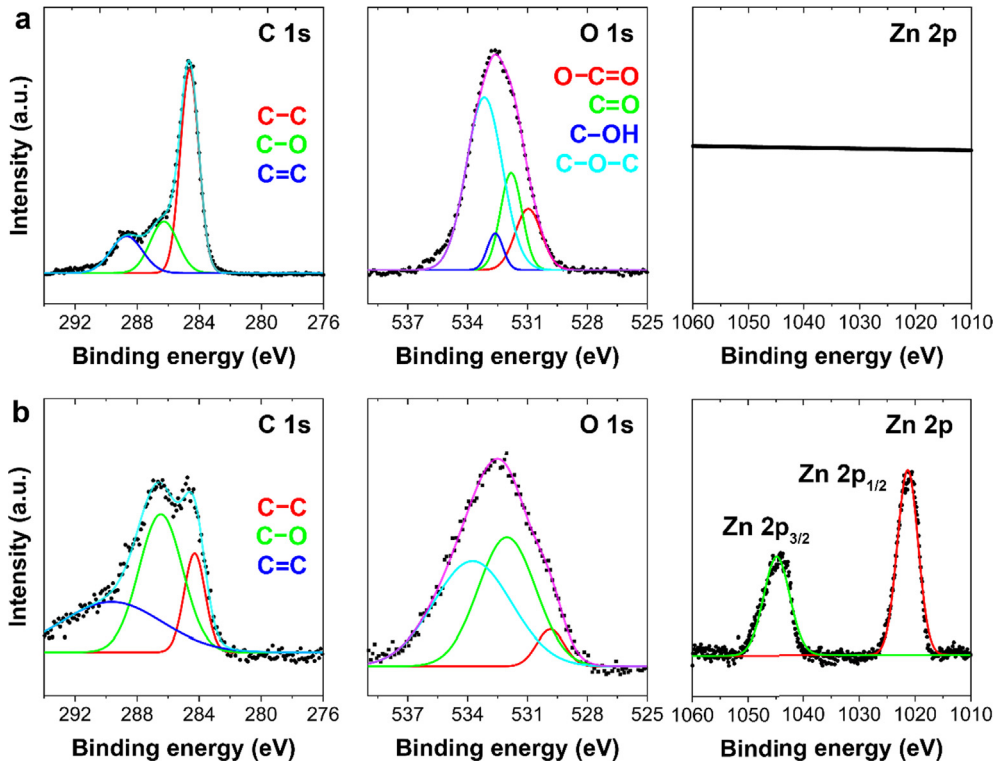

Fig. 3 X-ray photoelectron spectra of carbon (C) 1s, oxygen (O) 1s, and zinc (Zn) 2p of the (a) L-GO and (b) L-GO–ZnO electrodes.

Table 2 Data from the Brunauer–Emmett–Teller method observed in our study.

Anode	BET surface area (m^2/g)	Pore volume (cm^3/g)	Pore size (Å)
L-GO	280.1	0.222	31.5
L-GO-ZnO	12.8	0.023	91.9

Day 80. On Day 25, the L-GO–ZnO composite anode generated the highest voltage, 191 ± 4 mV, which is approximately 1.72 times greater than that obtained with the unmodified L-GO anode. That difference stemmed from not only the presence of a metal oxide, ZnO, in the modified anode, which significantly enhanced the electron transfer from the anode to cathode, but also the anode's high stability and biocompatibility with bacteria.

To determine the maximum power density (PD_{max}) and cell voltage behavior after stable performance was achieved, the polarization behavior of the MFCs was examined within 150 Ω to 10 kΩ of external resistance. The analysis also helped to evaluate the cells' design point (CDP), which is critical for assessing the performance of MFCs. As shown by the polarization curves in Fig. 5**b and c**, the L-GO–ZnO anode exhibited a significantly enhanced CDP, with a PD_{max} of 2.55 mW/m^2, a CD of 135.96 mA/m^2, and 155 mV generated at an external resistance of 150 Ω, compared with that of L-GO, with a PD_{max} of 0.1076 mW/m^2, a CD of 15.65 mA/m^2, and 119 mV generated at an external resistance of 1 kΩ. With less external resistance, the voltage destabilization rate increased, whereas with more external resistance (i.e., 10 kΩ) both electrodes demonstrated less current efficiency. The potential drop and slow stabilization at low amounts of external resistance may have derived from the effective discharge of electrons. After all, higher external resistance prevents electrons from moving as rapidly and easily toward the cathode, which diminished the power generated.

Among other results, the values of internal resistance observed were 2700 Ω and 710.8 Ω with the L-GO and L-GO–ZnO anodic MFC operations, respectively, and the L-GO–ZnO anode showed less external loss, less internal resistance, and less activation energy than the L-GO anode. The setup with less internal resistance demonstrated a high rate of electron movement, which led to a greater generation of electric current than internal resistance (Abazarian et al., 2016). In general, the internal resistance of MFCs depends upon (1) the electrode's nature and surface area, (2) its conductivity, (3) the distance between the anode and cathode, (4) the reaction on the electrode's surface, and (5) the electrolyte's concentration and/or nature. An external oxygen supply was also provided to enhance the reaction's cathodic rate and, in turn, stabilize the voltage at a typically high level of resistance (Sajana et al., 2017). Most researchers consider the oxygen supply to the cathode chamber in differentiating the aerated and non-aerated MFC processes under different conditions.

3.2.2. Cyclic voltammetry and electrochemical impedance spectroscopy characterization

Next, CV and EIS were applied to study the rate of electron transfer and the electrochemical behavior of the fabricated

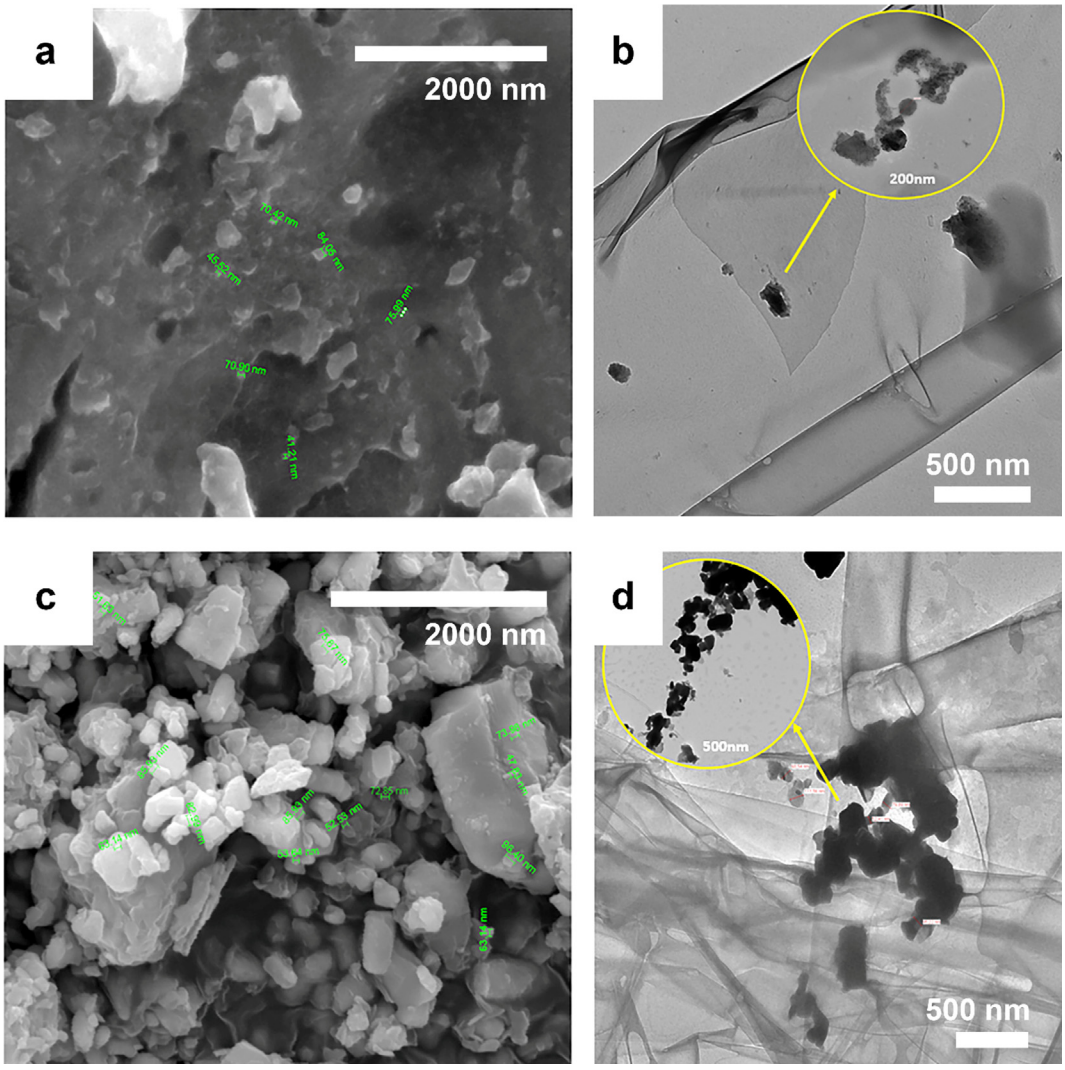

Fig. 4 (a and c) FE-SEM and (b and d) TEM micrographs of (a and b) L-GO and (c and d) the L-GO–ZnO composite.

anodes. As shown in Fig. 6**a**, the highest currents of the L-GO anode in the forward scan were 2.2×10^{-6} mA on Day 20, 3.0×10^{-6} mA on Day 40, 1×10^{-6} mA on Day 60, and 0.8×10^{-6} mA on Day 80. In the reverse scan, by contrast, the values were -6×10^{-6} mA on Day 20, -8.5×10^{-6} mA on Day 40, -1.2×10^{-5} mA on Day 60, and -2.3×10^{-5} mA on Day 80. Similarly, for the L-GO–ZnO anode, the values attained during the forward scan were 4.3×10^{-6} mA on Day 20, 4.0×10^{-6} mA on Day 40, 3.8×10^{-6} mA on Day 60, and 0.7×10^{-5} mA on Day 80 and in the reverse scan were -0.9×10^{-5} mA on Day 20, -1.9×10^{-5} mA on Day 40, -2.3×10^{-5} mA on Day 60, and -2.7×10^{-5} mA on Day 80 (Fig. 6**b**). The electrodes had the same geometrical area despite significantly different specific surface areas, of which the L-GO anodes was approximately 21.9 times greater. The maximum current registered during the forward and reverse scans indicate the highest oxidation and reduction rates during operation. For the L-GO–ZnO electrode, the current for oxidation and reduction processes peaked after Day 80 of operation, possibly due to the external supply of oxygen to the cathodic chamber, which may have enhanced the rate of electron discharge and neutralized the electrons before they approached the anode. The oxidation peak was also high due to the oil palm trunk sap, which has been recognized as an excellent source for bacteria (Liu et al., 2016).

Using the data, the specific capacitance (C_s) was determined for both electrodes. As shown in Table 3, the specific capacitance increased along with the operation time until peaking after Day 60 and thereafter decreasing. That increment during the first 60 days indicates the growth of healthy biofilm on the anode's surface. The anode's high capacitance occurred due to enhanced exoelectrogenic accumulation on the anode's surface, as also observed by Hong et al. (2011).

EIS Nyquist plots (Fig. 7) were investigated within the frequency range of 100 kHz to 100 mHz at an amplitude of 1.00 mV AC, which prevented the biofilm's detachment and decreased disturbances in the stable state. The fabricated L-GO and L-GO–ZnO anodes were presumably affected by diffusion and a kinetic reaction with the solution's resistance (R_s) and charge transfer resistance (R_{ct}) (Hung et al., 2019). The EIS plot revealed bent lines or irregular semicircles at higher frequencies, which correspond to a high rate of electron

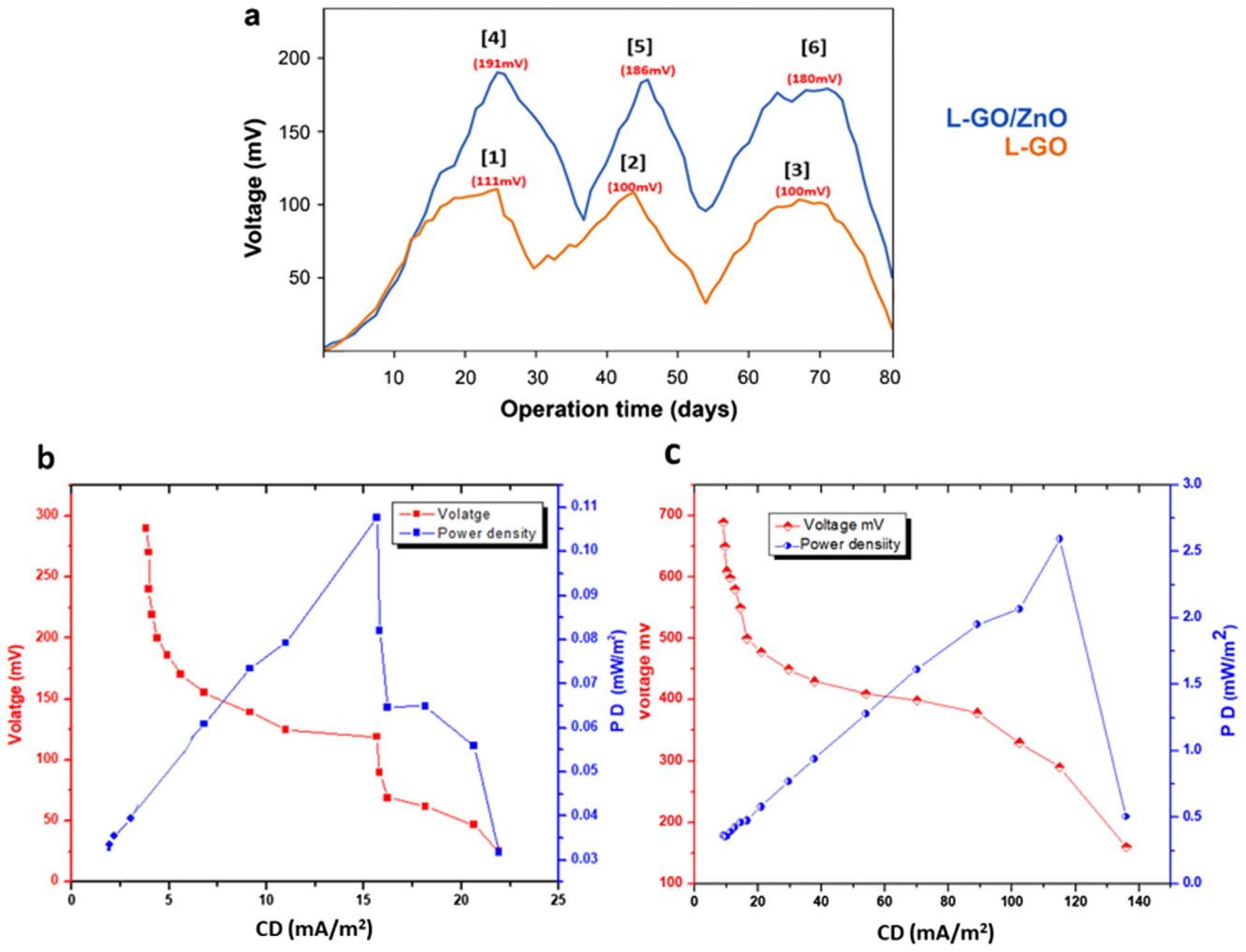

Fig. 5 (a) Time–voltage curve of MFCs in synthetic wastewater of the L-GO and modified L-GO–ZnO composite anodes (i.e., 1 kΩ external resistance) and polarization plot of (b) the L-GO anode and (c) L-GO–ZnO anode.

transfer, and straight or irregular lines at lower frequencies, which indicate good capacitive behavior. L-GO–ZnO demonstrated low charge transfer resistance in the electrolyte and a higher electronic mobility than the unmodified L-GO. The presence of high internal resistance in the L-GO anode indicated poor electronic mobility between the redox solution and electrodes. By comparison, the internal resistance of the L-GO–ZnO was lower, which suggested a high electron transfer to the redox solution and electrodes. The low R_{ct} in the case of L-GO–ZnO promoted the rate of kinetic reactions and concurrently reduced the electron transfer resistance. The fitted results were determined by using the Zview software. The L-GO-ZnO anode showed a lower R_{ct} value (0.02 Ω) than the L-GO anode (1.00 Ω). It indicated that L-GO-ZnO anode with active biofilms shows improved electron transfer capability. That aspect made the L-GO-ZnO anode in MFCs more prolific than the L-GO anode, which facilitated better energy efficiency.

3.2.3. Stability studies of anodes

The thermal, chemical, and mechanical stabilities of electrodes are critical factors for MFCs that determine long-term versus lack of operation. Currently, long-term stability is an emerging challenge in fabricating anodes, especially for MFCs, because some conditions can prolong the treatment of wastewater and production of energy. According to the literature, GO-based anodes usually demonstrate high mechanical, chemical, and thermal forms of stability (Mishra and Jain, 2016).

To examine the stability of the synthesized L-GO and L-GO–ZnO, thermal gravimetric analysis was first performed after Day 80 of operation in order to evaluate the thermal stability of the L-GO and L-GO–ZnO electrodes. As shown in **Fig. S3a**, after Day 80 at room temperature (25 °C) the L-GO and L-GO–ZnO anodes showed 5% and 1% weight loss, respectively. From 25 to 100 °C, 24% and 6% total weight loss was observed for L-GO and L-GO–ZnO, also respectively, primarily because water adhered to the anode's surface. However, from 25 to 900 °C, L-GO and L-GO–ZnO respectively exhibited 56% and 34% total weight loss. L-GO–ZnO exhibited excellent thermal stability, thereby suggesting its eligibility to operate at moderate and relatively high temperatures.

The chemical stability of the anodes was explored via compositional and morphological analyses after Day 80 of operation. Although the full results are discussed in Section 3.2.5, it

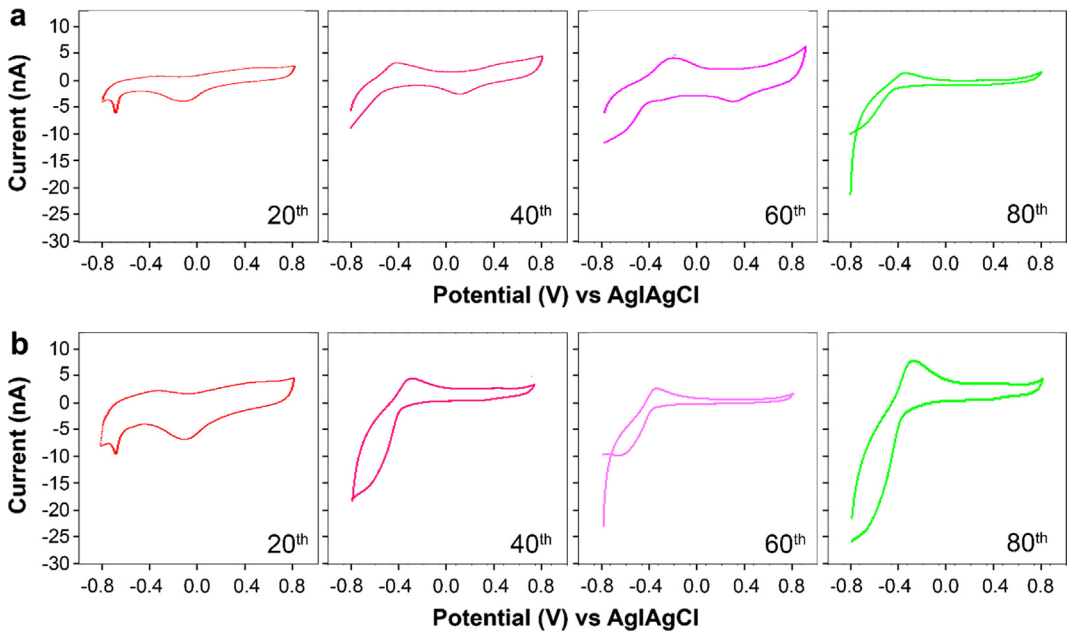

Fig. 6 Cyclic voltammograms recorded at a scan rate of 20 mV s^{-1} on the (a) L-GO and (b) L-GO–ZnO electrodes using a phosphate buffer solution (pH = 7.0).

Table 3 Specific capacitances of fabricated L-GO and L-GO–ZnO on Days 20, 40, 60, and 80.

Time interval (Days)	Capacitance (mF/g)	
	L-GO-based anode in MFCs	L-GO-ZnO-based anode in MFCs
20	0.01	0.02
40	0.02	0.04
60	0.04	0.06
80	0.00	0.01

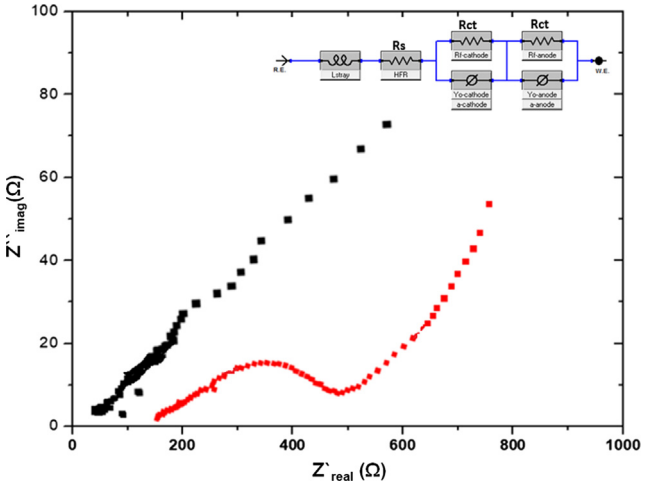

Fig. 7 Nyquist plots (EIS) for the (a) L-GO and (b) L-GO–ZnO electrodes.

can be concluded that the chemical stability of L-GO and L-GO–ZnO was relatively high, because no chemical hazards or toxic elements appeared in the electrochemical media, and significant morphological changes were detected on the surface of the anodes after such long-term operation.

A mechanical test was additionally performed to measure the mechanical strength of the anodes, because continuous, long-term operation, especially at an industrial scale, can damage electrodes. Graphene derivatives usually possess considerable mechanical strength (e.g., 130 GPa reported by Papageorgiou et al. (2017), and as shown in **Fig. S3b**, L-GO could sustain a maximum pressure of 20 psi, whereas L-GO–ZnO could sustain a pressure of 30 psi. At higher pressures, both electrodes were broken or damaged. Such results suggest that both electrodes exhibited relatively high mechanical strength.

3.2.4. Removal efficiency and bacterial identification studies

As various studies have shown, MFCs are ideal for remediating wastewater, and graphene-based electrodes can enhance the generation of energy and the efficient remediation of toxic metals from wastewater (Kumar et al., 2019; Zhang et al., 2018; Yaqoob et al., 2020e). Considering such evidence, the potential of two GO-based anodes to remove 100 ppm Cd (II) from synthetic wastewater was investigated in our study.

As shown in Table 4, the removal efficiencies of the L-GO and L-GO–ZnO anodes up to Day 80 of operation were 83.5% and 90.0%, respectively. The high performance of L-GO–ZnO could be attributed to its high conductivity, which offers exceptional stability for healthy bacterial respiration due to the improved transfer of electrons and protons. By contrast, the unmodified L-GO anode's surface failed to allow the bacteria to breath rapidly enough to release the electrons and protons. In both cases, the adsorptive properties of graphene-based material attracted Cd (II) ions to the surface,

Table 4 Overview of the removal of Cd (II) with the modified L-GO and unmodified L-GO anodes.

Inoculum source	Initial concentration of Cd (II) (ppm)	Organic substrate	Temperature (°C)	Electrode		Operational time (Days)	Removal efficiency (%)
				Anode	Cathode		
Synthetic wastewater	100	Oil palm trunk sap	25 ± 1	L-GO	Graphite rod	0	0.00
						10	17.00
						20	30.50
						40	48.00
						60	67.00
						70	80.20
						80	83.50
				L-GO-ZnO	Graphite rod	0	0.00
						10	19.00
						20	40.70
						40	60.00
						60	78.31
						70	87.45
						80	90.00

where exoelectrogenic biofilms removed the Cd (II) ions during bacterial respiration. In the first 20 days of operation, the unmodified GO anode's removal efficiency was 1.3 times greater than the L-GO anodes. In general, removal efficiency depends heavily upon the operating conditions, including pH level, temperature, and water matrix effects. In our study, 90% of Cd (II) was removed in an oxic environment at 25 °C and a pH of 6.41 using L-GO–ZnO as the anode and oil palm trunk sap as the organic substrate. That moderate temperature and pH level were selected to capture their performance under realistic, green, competitive conditions. The result was comparable, if not superior, to the outcomes of other Cd (II) removals (i.e., 100 ppm) from synthetic wastewater by using MFCs reported in the literature.

Next, the bacterial communities' composition in both the L-GO and L-GO–ZnO anodes was determined by studying clone libraries (**Table S1**). Both electrodes hosted a diversity of exoelectrogenic bacterial species, which shows promise for MFCs as a material for remediating toxic pollutants as well as generating energy. A particularly efficient species was *Lysinibacillus fusiformis*, detected on the surface of both anodes, which exhibits exceptional resistance to Cd (II) and other metallic ions such as lead, copper, and zinc (Mathivanan et al., 2016; Nandy et al., 2013; Páez-Vélez et al., 2019). Beyond that, *Lysinibacillus sphaericus*, *Escherichia coli*, Enterobacter spp., *Chryseobacterium gleum*, *Bacillus* spp., *Citrobacter youngae*, and *Klebsiella pneumoniae* are other well-known exoelectrogenic bacterial species that excel in remediating metals and generating energy via MFCs (Feng et al., 2014; Tkach et al., 2015). **Table S1** presents an exhaustive list of the principal species responsible for Cd (II)'s removal from wastewater and generation of energy in the MFC-based approach.

3.2.5. Biofilm morphology and its biocompatibility

Also known as a "city of bacteria," biofilm is produced in natural circumstances during bioelectrochemical process. The biofilm's matrix consisted of water (97%), bacterial cells (2–5%), extracellular polymeric substance (EPS, 3–6%), and several trace mineral ions (Di Martino, 2018). The most important component was EPS, which aggregates the cells on biofilms due to its composition of proteins (1–60%), polysaccharides (40–95%), lipids (40%), and nucleic acids (10%)(Kumar et al., 2011). EPS was extraordinarily hydrated such that it can hold water molecules via hydrogen bonding and its quantity in biofilms determined their age. Of course, bacteria consortia and different environmental parameters, including pH and temperature, also affected the formation of biofilms. For that reason, it was necessary to evaluate the biofilm's morphology to gauge the performance of energy generation and Cd (II) removal.

As shown in Fig. 5**a**, in both L-GO and L-GO–ZnO the initial voltage was rather small (i.e., 1 mV and 3 mV, respectively). Over time, however, the daily intake of organic substrate by the bacterial community produced a biofilm and enabled the bacterial colonies to work as electrochemically active agents in releasing electrons and protons. During the reaction, the capacity of bacterial growth on the anodes was examined by running the reaction in three cycles. The greatest energy was observed in the first cycle (i.e., 111 mV and 191 mV for L-GO and L-GO–ZnO, respectively) up to Day 25. Again, the removal rate increased with the passage of time and peaked at 83.5% and 90% for L-GO and L-GO–ZnO, respectively, because the bacteria present on the biofilm effectively reduced the metal's toxic effect.

SEM analysis was conducted to characterize the bacterial colonies on the surface of the anodes (Fig. 8). The treated cathode surface was also analyzed to determine the bacterial presence on a graphite rod (i.e., cathode electrode). As shown in Fig. 8, the untreated anode did not exhibit any type of biofilm on its surface. However, after Day 80, several specific bacteria colonies were clearly identifiable on the surface of the treated anode and were considered to be responsible for the generation of energy and Cd (II)'s removal. Overall, the results indicated that a limited formation of biofilm promotes the generation of energy. Sasaki et al. (2019) also demonstrated that the limited formation of biofilm on an anode's surface facilitates the generation of energy and the efficiency of removal. The high biomass on the anode's surface affected the EPS's composition,

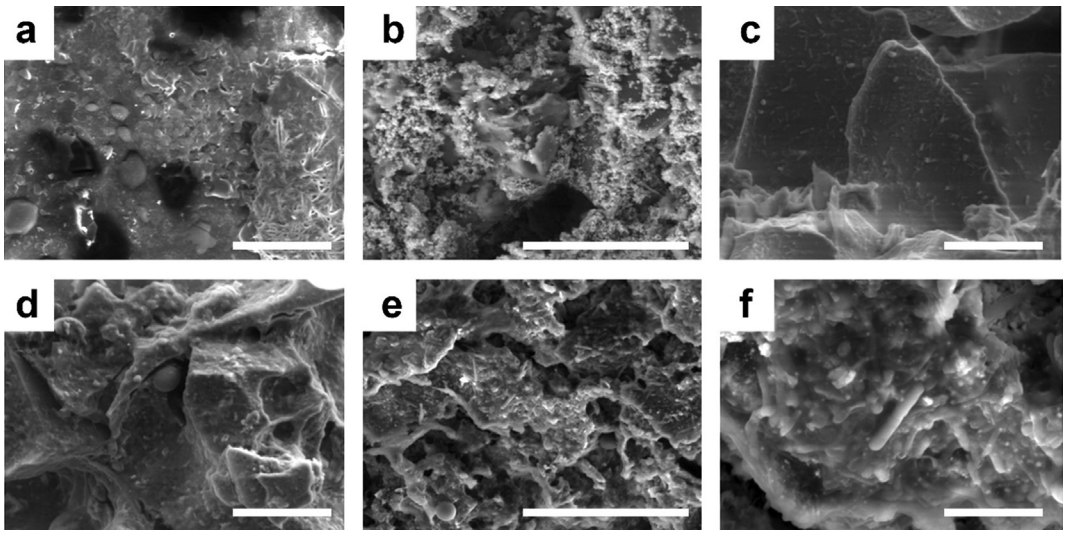

Fig. 8 SEM images of the untreated (a) L-GO anode, (b) cathode (i.e., graphite rod), and (c) L-GO–ZnO anode; and of the treated (d) L-GO anode, (e) cathode (i.e., graphite rod), and (f) L-GO–ZnO anode. Scale bar: 30 μm.

which translated into less energy generation. MFCs thus seem to support ecofriendly approaches to generating energy without producing hazardous gases or by-products. Last, SEM and EDX, performed to analyze the biofilm's composition (**Fig. S4**), revealed no toxic elements on the anode's surface, which would have hindered the growth and production of bacteria and, in turn, the formation of biofilm.

3.2.6. Energy generation, transportation, and metal reduction mechanism of the present study

Before metal reduction via bacterial species, energy generation and its transportation mechanism need to be understood. Bacterial species work as biocatalysts in MFCs approach, in which provided organic substrate is oxidized by bacterial species to produce electrons and protons. Several bacterial species are well known exoelectrogens and metal reducing species such as *E. coli, Rhodoferax ferrireducens*, *Clostridium butyricum*, *Geobacter* spp. *Aeromonas hydrophila, Bacillus, Shewanella* sp. and *Klebsiella pneumoniae* (Yaqoob et al., 2020c). However, in the present study we used oil palm trunk sap as an organic substrate that was oxidized by bacterial species to generate the electrons and protons. The oil palm trunk sap was converted into simple glucose, which was then further oxidized by bacterial species. Yamada et al. (2010) reported that oil palm sap contains more than 90% total sugar content. The oil palm trunk sap is easily and freely available in ASEAN countries and is already proven to be a good fuel source for bacterial activities (such as the Krebs cycle process) (Yaqoob et al., 2020b). The biochemical reaction of the present study can be written as:

Anodic reaction: Oil palm trunck sap

$$\rightarrow C_6H_{12}O_6 + 6H_2O \rightarrow 6CO_2 + 24H^+ + 24e^-$$

Cathodic reaction: $24H^+ + 24e^- + 6O_2 \rightarrow 12H_2O$

Overall reaction: $C_6H_{12}O_6 + 6O_2$

$$\rightarrow 6CO_2 + 6H_2O + \text{Electricity} + \text{Biomass}$$

The produced biofilm around the anode surface oxidized and generated electron and protons. The protons were transferred directly through PEM and the electrons were used on the outer circuit to reach the cathode for a reduction reaction. Two major mechanisms (direct and indirect electron transfer) were involved in the transportation of electrons from the bacterial cells to the anode surface before transferring toward the cathode through the outer circuit, as shown in Fig. 9**.**

- Direct electron transfer is further classified into two processes: the electron transportation through conductive pili-type bacterial species or utilizing the redox-active proteins to transfer electrons. The *Aeromonas hydrophila, Acinetobacter radioresistens strains, Klebsiella pneumoniae* and many others contain conductive pili. Pili is part of the bacterium body that is conductive like metal and transfers electrons directly to any conductive material. According to the present study, the bacterial identification process showed the species that belong to the conductive pili-type bacterial class. This indicates that the present study followed the direct electron transfer mechanism. The presence of conductive pili-type species is also confirmed in the SEM images of the treated anode. Fig. 8 shows the tube/rod filamentous structures that belong to conductive pili-type species according to pervious literature (He et al., 2011; Ishii et al., 2008; Zhang et al., 2008). Further, in direct electron transfer the utilization of redox-active proteins are also commonly found in *Geobacter sulfurreducens*. This can produce self- redox-active proteins to use as a transferring medium. Some redox active proteins are OmcE, OmcZ, OmcS, OmcB, and OmcT and are mostly reported (Lebedev et al., 2015; Santos et al., 2015; Shang et al., 2015).
- The indirect electron transfer mechanism uses oxidized/reduced soluble electron shuttles. *Geobacteraceae* and *Desulfuromonadaceae* mainly followed this mechanism to transfer electrons (Vargas et al., 2013).

On the other side, the reduction mechanism of Cd (II) to Cd also occurred. As a reduction result, Cd (II) to $Cd_{(s)}$, means the

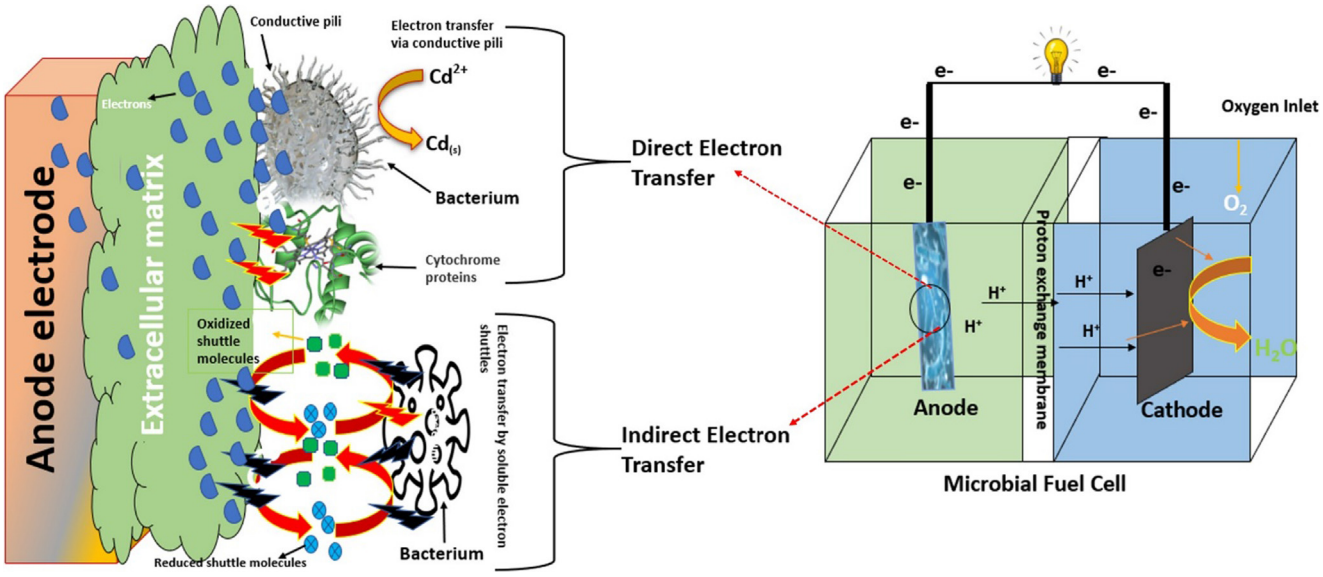

Fig. 9 Electron transfer mechanism from bacterial cell to the anode in MFCs.

soluble state of metal ions is converted into the insoluble solid state of the Cd. It is less toxic as compared to the soluble state of Cd. The reduction of Cd (II) to Cd can be written as:

$$Cd^{2+} + 2e^{-} \; Cd_{(s)}$$

$$2Cd^{2+} + 2H_2O \; 2CdO + 4H^{+}$$

$$CdO + 2e^{-} + 2H^{+} \; Cd_{(s)} + H_2O$$

4. Comparative discussion of electrodes with pervious literature

The preparation of the cost-effective and high-quality-based material for anode fabrication is a current topic in MFCs. Several factors are involved in the development of anodes to boost their performance in conductivity, durability, mechanical, thermal, and chemical biocompatibility toward the living microorganism in MFCs operation. According to the present results, both anodes show high mechanical, chemical and biocompatibility as discussed in above sections. The SEM images of the biofilm around both anodes show the chemical compatibility for bacterial growth. Similarly, the rate of electron transportation was observed in Fig. 5 which demonstrates the excellent outcomes. The observed durability of both anodes was 80 days in continuous operation. Each electrode delivered a maximum 111 mV (L-GO) and 191 mV (L-GO-ZnO) voltage during three cycles in a continuous mode of operation. The rate of electron transfer from anode to cathode was found to be quite good as compared to the pervious latest literature as presented in Table 5**.** The delivered PD_{max} was 0.1076 mW/m^2, (L-GO) and 2.55 mW/m^2 (L-GO-ZnO) while the maximum CD was 15.65 mA/m^2 (L-GO) and 135.96 mA/m^2 (L-GO-ZnO). The maximum CD and PD showed there was effective electron transportation for 80 days, which corresponds with the durability of the anodes. Each operation was treated with three cycles and each showed high durability during the replication of the results. The same trend was followed by several researchers to explain the durability and comparison profile of the prepared anodes (Gnana kumar et al., 2014; Kirubaharan et al., 2019; Kirubaharan et al., 2015; Kirubaharan et al., 2016; Senthilkumar et al., 2019). For example, Senthil et al. (Senthilkumar et al., 2020) fabricated the waste-derived 3D-carbon aerogel-ceria-nitrogen doped reduced graphene oxide based anode electrode. The stated durability of their anode was 360 h in continuous batch. Similarly, a comparative profile on the removal of toxic metal is presented in **Table S2.** The present archived removal efficiency was 90%, which is quite higher compared to previous literature. There was not much work reported on the removal of CD (II) through MFCs as a synthetic wastewater inoculation source. The reason for high removal efficiency and energy generation/transportation is the presence of the conductive, biocompatible electrode and highly favorable oil palm trunk sap as an organic substrate.

5. Conclusion

The present study tries to highlight the usage of biomass in improving the performance of MFCs. This study offers a triple-edge approach whereby in the effort of improving energy transmission and water treatment, not to mention at the same time the problem of accumulation of biomass can be reduced. The complete theme of MFCs operations is well summarized in a systematic way. This paper is the first (to the best of the authors knowledge) to have a comprehensive study on the preparation of anode by using a local waste material especially oil palm empty fruit bunch. Furthermore, this paper also is the first to report on the utilization of waste-derived organic waste (oil palm trunk sap) as an organic substrate in the removal of Cd (II) from synthetic wastewater.

The synthesis of material from waste sources to fabricate promising anodes and electrodes, namely L-GO, for MFCs to improve the generation of energy and efficiency of removing heavy metals from wastewater. To enhance the anode's performance, ZnO nanoparticles were incorporated into L-GO as a means to fabricate a composite material, L-GO–ZnO. Both materials were characterized by different analytical techniques in order to study their structural and morphological prop-

Table 5 Comparative summary of electrode durability and efficiency.

Anode electrode	Size of electrode (h × r)	Surface area of anode	Inoculation source	Durability (days)	Current density (mA/m^2)	References
Fe_3O_4/AC[1]/SSM[2]	4 cm × 3 cm	7 cm^2	*Pre-acclimated Effluent*	5	1.9 mA/m^2	(Peng et al., 2013)
CP[3]/HAPNW[4]	3.14 cm × 2.5 cm	88.5 cm^2	*Shewanella Loihica*	2.2	2.9 mA/cm^2	(Zhao et al., 2011)
AC[1]/PANI[5]/D-CSA[6]/GF[7]	Length:100–200 nm, Diameter: 80 nm	–	Domestic Wastewater	6.2	110 mA/m^2	(Scott et al., 2007)
CNT[8]/CC[9]	6 cm × 3.5 cm	208.81 cm^2	Wastewater	8–9	65 mA/m^2	(Tsai et al., 2009)
Graphene/PEDOT[10]/CP[3]	2 cm × 2.5 cm	10 cm^2	*Escherichia coli*	24	3.59 mA/m^2	(Wang et al., 2013)
PEI[11]/GF[12]	–	7 cm^2	*Saccharomyces cerevisiae*	5	–	(Christwardana et al., 2018)
GO[13]	7.5 cm × 1.2 cm	71.0 cm^2	Synthetic wastewater	40	24.56 mA/m2	(Yaqoob et al., 2021)
GO-PANI[14]	7.5 cm × 1.2 cm	71.0 cm^2	Synthetic wastewater	40	87.71 mA/m2	(Yaqoob et al., 2021)
L-GO[15]	8.0 cm × 1.3 cm	76.0 cm^2	Synthetic wastewater	80	15.65 mA/m^2	Present work
L-GO-ZnO composite	8.0 cm × 1.3 cm	76.0 cm^2	Synthetic wastewater	80	135.96 mA/m^2	Present work

[1] Activated carbon.
[2] Stainless steel meshes.
[3] Carbon paper.
[4] Hydroxylated and aminated polyaniline nanowire.
[5] Polyaniline.
[6] D-camforsulfonic Acid.
[7] Graphite felt.
[8] Carbon nanotubes.
[9] Carbon cloth.
[10] Poly(3,4-ethylenedioxythiophene).
[11] Polyethyleneamine.
[12] Graphite.
[13] Graphene oxide.
[14] Polyaniline.
[15] Lignin-graphene oxide.

erties. Among the results, the fabricated bioinspired anode demonstrated excellent energy generation and Cd (II) removal during a continuous 80-day period of operation with MFCs compared with the conventional anode material. In follow-up, different techniques, including CV, EIS, and anode stability analysis, were used to assess the polarization behavior, specific capacitance, and factors of biocompatibility of the fabricated anode. The techniques revealed a diversity of bacterial species on the cells, which indicate that MFCs may be useful for remediating heavy metals and generating energy on an industrial scale. Going forward, researchers should examine anode–bacteria interaction to further illuminate the possibilities of using MFCs on such a scale.

CRediT authorship contribution statement

Asim Ali Yaqoob: Methodology, Writing - original draft, Writing - review & editing, Visualization, Investigation. **Albert Serrà:** Methodology, Writing - original draft, Writing - review & editing, Visualization, Investigation. **Mohamad Nasir Mohamad Ibrahim:** Conceptualization, Supervision, Funding acquisition. **Amira Suriaty Yaakop:** Conceptualization.

Declaration of Competing Interest

The authors declare that they have no known competing financial interests or personal relationships that could have appeared to influence the work reported in this paper.

Acknowledgments

This article was financially supported by Universiti Sains Malaysia (Malaysia) under research grant no. 203/PKIMIA/6740073. Dr. Mohamad Nasir Mohamad Ibrahim wishes to gratefully acknowledge Dr. Rokiah Hashim's research group from the School of Industrial Technology, Universiti Sains Malaysia, 11800 Minden, Penang, Malaysia, for providing the oil palm trunk sap.

Appendix A. Supplementary material

Supplementary data to this article can be found online at https://doi.org/10.1016/j.arabjc.2021.103121.

References

Abazarian, E., Gheshlaghi, R., Mahdavi, M.A., 2016. The effect of number and configuration of sediment microbial fuel cells on their performance in an open channel architecture. J. Power Sourc. 325, 739–744.

Al-Gaashani, R., Najjar, A., Zakaria, Y., Mansour, S., Atieh, M., 2019. XPS and structural studies of high quality graphene oxide and reduced graphene oxide prepared by different chemical oxidation methods. Ceram Intern. 45 (11), 14439–14448.

Anandhavelu, S., Thambidurai, S., 2013. Single step synthesis of chitin/chitosan-based graphene oxide–ZnO hybrid composites for better electrical conductivity and optical properties. Electrochim. Act. 90, 194–202.

Chauhan, P.S., Kant, R., Rai, A., Gupta, A., Bhattacharya, S., 2019. Facile synthesis of ZnO/GO nanoflowers over Si substrate for improved photocatalytic decolorization of MB dye and industrial wastewater under solar irradiation. Mater. Sci. Semicond. Process. 89, 6–17.

Christwardana, M., Frattini, D., Accardo, G., Yoon, S.P., Kwon, Y., 2018. Effects of methylene blue and methyl red mediators on performance of yeast based microbial fuel cells adopting polyethylenimine coated carbon felt as anode. J. Power Sourc. 396, 1–11.

Di Martino, P., 2018. Extracellular polymeric substances, a key element in understanding biofilm phenotype. AIMS microb. 4 (2), 274.

Durmus, Z., Kurt, B.Z., Durmus, A., 2019. Synthesis and characterization of graphene oxide/zinc oxide (GO/ZnO) nanocomposite and its utilization for photocatalytic degradation of basic Fuchsin dye. Chem. Sel. 4 (1), 271–278.

Feng, C., Li, J., Qin, D., Chen, L., Zhao, F., Chen, S., Hu, H., Yu, C.-P., 2014. Characterization of exoelectrogenic bacteria Enterobacter strains isolated from a microbial fuel cell exposed to copper shock load. PLoS ONE 9, (11) e113379.

Gnana Kumar, G., Kirubaharan, C.J., Udhayakumar, S., Karthikeyan, C., Nahm, K.S., 2014. Conductive polymer/graphene supported platinum nanoparticles as anode catalysts for the extended power generation of microbial fuel cells. Indust. Eng. Chem. Res. 53 (43), 16883–16893.

He, G., Gu, Y., He, S., Schröder, U., Chen, S., Hou, H., 2011. Effect of fiber diameter on the behavior of biofilm and anodic performance of fiber electrodes in microbial fuel cells. Bioresour. Technol. 102 (22), 10763–10766.

Hong, Y., Call, D.F., Werner, C.M., Logan, B.E., 2011. Adaptation to high current using low external resistances eliminates power overshoot in microbial fuel cells. Biosens. Bioelectron. 28 (1), 71–76.

Hung, Y.-H., Liu, T.-Y., Chen, H.-Y., 2019. Renewable coffee waste-derived porous carbons as anode materials for high-performance sustainable microbial fuel cells. ACS Sust. Chem. Eng. 7 (20), 16991–16999.

Ishii, S.I., Shimoyama, T., Hotta, Y., Watanabe, K., 2008. Characterization of a filamentous biofilm community established in a cellulose-fed microbial fuel cell. Bmc Microbiol. 8 (1), 1–12.

Kannan, M., 2016. Current status, key challenges and its solutions in the design and development of graphene based ORR catalysts for the microbial fuel cell applications. Biosens. Bioelectron. 77, 1208–1220.

Karthikeyan, R., Wang, B., Xuan, J., Wong, J.W., Lee, P.K., Leung, M.K., 2015. Interfacial electron transfer and bioelectrocatalysis of carbonized plant material as effective anode of microbial fuel cell. Electrochimica Act. 157, 314–323.

Kirubaharan, C.J., Kumar, G.G., Sha, C., Zhou, D., Yang, H., Nahm, K.S., Raj, B.S., Zhang, Y., Yong, Y.-C., 2019. Facile fabrication of Au@ polyaniline core-shell nanocomposite as efficient anodic catalyst for microbial fuel cells. Electrochimica Act. 328, 135136.

Kirubaharan, C.J., Santhakumar, K., Senthilkumar, N., Jang, J.-H., 2015. Nitrogen doped graphene sheets as metal free anode catalysts for the high performance microbial fuel cells. Int. J. Hydr. Eng. 40 (38), 13061–13070.

Kirubaharan, C.J., Yoo, D.J., Kim, A.R., 2016. Graphene/poly (3, 4-ethylenedioxythiophene)/Fe3O4 nanocomposite–An efficient oxygen reduction catalyst for the continuous electricity production from wastewater treatment microbial fuel cells. Int. J. Hydrogen Energ. 41 (30), 13208–13219.

Kumar, M.A., Anandapandian, K.T.K., Parthiban, K., 2011. Production and characterization of exopolysaccharides (EPS) from biofilm forming marine bacterium. Brazilian Arch. Biol. Technol. 54 (2), 259–265.

Kumar, S.S., Kumar, V., Malyan, S.K., Sharma, J., Mathimani, T., Maskarenj, M.S., Ghosh, P.C., Pugazhendhi, A., 2019. Microbial fuel cells (MFCs) for bioelectrochemical treatment of different wastewater streams. Fuel 254, 115526.

Lebedev, N., Mahmud, S., Griva, I., Blom, A., Tender, L.M., 2015. On the electron transfer through Geobacter sulfurreducens PilA protein Part B Polymer physics. J. Polym. Sci. 53, 1706–1717.

Li, W., Jiang, X., Yang, H., Liu, Q., 2015. Solvothermal synthesis and enhanced CO2 adsorption ability of mesoporous graphene oxide-ZnO nanocomposite. Appl. Surf. Sci. 356, 812–816.

Li, X., Sun, P., Yang, T., Zhao, J., Wang, Z., Wang, W., Liu, Y., Lu, G., Du, Y., 2013. Template-free microwave-assisted synthesis of ZnO hollow microspheres and their application in gas sensing. CrystEngComm 15 (15), 2949–2955.

Liu, H., Logan, B.E., 2004. Electricity generation using an air-cathode single chamber microbial fuel cell in the presence and absence of a proton exchange membrane. Environ. Sci. Technol. 38 (14), 4040–4046.

Liu, L., Chou, T.-Y., Lee, C.-Y., Lee, D.-J., Su, A., Lai, J.-Y., 2016. Performance of freshwater sediment microbial fuel cells: Consistency. Int. J. Hydrogen Energ. 41 (7), 4504–4508.

Logan, B.E., Rabaey, K., 2012. Conversion of wastes into bioelectricity and chemicals by using microbial electrochemical technologies. Science 337 (6095), 686–690.

Mathivanan, K., Rajaram, R., Balasubramanian, V., 2016. Biosorption of Cd (II) and Cu (II) ions using Lysinibacillus fusiformis KMNTT-10: equilibrium and kinetic studies. Desal. Water Treat. 57 (47), 22429–22440.

Mishra, P., Jain, R., 2016. Electrochemical deposition of MWCNT-MnO2/PPy nano-composite application for microbial fuel cells. Int. J. Hydrogen Energ. 41 (47), 22394–22405.

Nandy, A., Kumar, V., Kundu, P.P., 2013. Utilization of proteinaceous materials for power generation in a mediatorless microbial fuel cell by a new electrogenic bacteria Lysinibacillus sphaericus VA5. Enzyme Microb. Technol. 53 (5), 339–344.

Páez-Vélez, C., Rivas, R.E., Dussán, J., 2019. Enhanced gold biosorption of Lysinibacillus sphaericus CBAM5 by encapsulation of bacteria in an alginate matrix. Metal. 9 (8), 818.

Papageorgiou, D.G., Kinloch, I.A., Young, R.J., 2017. Mechanical properties of graphene and graphene-based nanocomposites. Prog. Mater. Sci. 90, 75–127.

Pareek, A., Sravan, J.S., Mohan, S.V., 2019. Fabrication of three-dimensional graphene anode for augmenting performance in microbial fuel cells. Carbon Resour. Conver. 2 (2), 134–140.

Peng, X., Yu, H., Ai, L., Li, N., Wang, X., 2013. Time behavior and capacitance analysis of nano-Fe3O4 added microbial fuel cells. Bioresour. Technol. 144, 689–692.

Sajana, T., Ghangrekar, M., Mitra, A., 2017. In situ bioremediation using sediment microbial fuel cell. J. Hazard, Toxic, Radioact. Wast. 21 (2), 04016022.

Santos, T.C., Silva, M.A., Morgado, L., Dantas, J.M., Salgueiro, C. A., 2015. Diving into the redox properties of Geobacter sulfurreducens cytochromes: a model for extracellular electron transfer. Dalton Transact. 44 (20), 9335–9344.

Sasaki, D., Sasaki, K., Tsuge, Y., Kondo, A., 2019. Less biomass and intracellular glutamate in anodic biofilms lead to efficient electricity generation by microbial fuel cells. Biotechnol. biofuel. 12 (1), 72.

Scott, K., Rimbu, G., Katuri, K., Prasad, K., Head, I., 2007. Application of modified carbon anodes in microbial fuel cells. Process Saf. Environ. Protect. 85 (5), 481–488.

Sekeri, S.H., Ibrahim, M.N.M., Umar, K., Yaqoob, A.A., Taib, M.N. A.M., Hussin, M.H., Othman, M.B.H., Malik, M.F.I.A., 2020. Preparation and characterization of nanosized lignin from oil palm (Elaeis guineensis) biomass as a novel emulsifying agent. Int. J. Bio Macromole. 164, 3114–3124.

Senthilkumar, N., Aziz, M.A., Pannipara, M., Alphonsa, A.T., Al-Sehemi, A.G., Balasubramani, A., 2020. Waste paper derived three-dimensional carbon aerogel integrated with ceria/nitrogen-doped reduced graphene oxide as freestanding anode for high performance and durable microbial fuel cells. Biopro. Biosyst. Eng. 43 (1), 97–109.

Senthilkumar, N., Pannipara, M., Al-Sehemi, A.G., 2019. PEDOT/NiFe 2 O 4 nanocomposites on biochar as a free-standing anode for high-performance and durable microbial fuel cells. New J. Chem. 43 (20), 7743–7750.

Shakeel, N., Ahamed, M.I., Kanchi, S., Kashmery, H.A., 2020. Green synthesis of Zno nanoparticles decorated on polyindole functionalized-Mcnts and used as anode material for enzymatic biofuel cell applications. Sci. Rep. 10 (20), 1–10.

Shang, B., Liu, Y., Jiang, S.-J., Liu, Y., 2015. Prognostic value of tumor-infiltrating FoxP3+ regulatory T cells in cancers: a systematic review and meta-analysis. Sci. Rep. 5 (1), 1–9.

Tkach, O., Liu, L., Wang, A., 2015. Electricity generation by Enterobacter sp. of single-chamber microbial fuel cells at different temperatures. J. Clean Energy Technol. 4 (1), 36.

Tsai, H.-Y., Wu, C.-C., Lee, C.-Y., Shih, E.P., 2009. Microbial fuel cell performance of multiwall carbon nanotubes on carbon cloth as electrodes. J Power Sourc. 194 (1), 199–205.

Umar, K., Aris, A., Parveen, T., Jaafar, J., Majid, Z.A., Reddy, A.V. B., Talib, J., 2015. Synthesis, characterization of Mo and Mn doped ZnO and their photocatalytic activity for the decolorization of two different chromophoric dyes. App. Catal. A: Gen. 505, 507–514.

Vardhan, K.H., Kumar, P.S., Panda, R.C., 2019. A review on heavy metal pollution, toxicity and remedial measures: Current trends and future perspectives. J. Mol. Liq. 290, 111197.

Vargas, M., Malvankar, N.S., Tremblay, P.-L., Leang, C., Smith, J.A., Patel, P., Synoeyenbos-West, O., Nevin, K.P., Lovley, D.R., 2013. Aromatic amino acids required for pili conductivity and long-range extracellular electron transport in Geobacter sulfurreducens. MBio. 4 (2).

Wang, R., Liu, D., Yan, M., Zhang, L., Chang, W., Sun, Z., Liu, S., Guo, C., 2019. Three-dimensional high performance free-standing anode by one-step carbonization of pinecone in microbial fuel cells. Bioresour. Technol. 292, 121956.

Wang, Y., Zhao, C.-E., Sun, D., Zhang, J.-R., Zhu, J.-J., 2013. A graphene/poly (3, 4-ethylenedioxythiophene) hybrid as an anode for high-performance microbial fuel cells. ChemPlusChem. 78 (8), 823.

Xu, S., Fu, L., Pham, T.S.H., Yu, A., Han, F., Chen, L., 2015. Preparation of ZnO flower/reduced graphene oxide composite with enhanced photocatalytic performance under sunlight. Ceram Inter. 41 (3), 4007–4013.

Yamada, H., Tanaka, R., Sulaiman, O., Hashim, R., Hamid, Z., Yahya, M., Kosugi, A., Arai, T., Murata, Y., Nirasawa, S., 2010. Old oil palm trunk: a promising source of sugars for bioethanol production. Biomass Bioenerg. 34 (11), 1608–1613.

Yang, C., Chen, M., Qian, Y., Zhang, L., Lu, M., Xie, X., Huang, L., Huang, W., 2019. Packed anode derived from cocklebur fruit for improving long-term performance of microbial fuel cells. Sci. China Mater. 62 (5), 645–652.

Yaqoob, A.A., Ibrahim, M.N.M., Rodríguez-Couto, S., 2020a. Development and modification of materials to build cost-effective anodes for microbial fuel cells (MFCs): An overview. Biochem. Eng. J. 164, 107779.

Yaqoob, A.A., Ibrahim, M.N.M., Yaakop, A.S., Umar, K., Ahmad, A., 2020b. Modified Graphene Oxide Anode: A Bioinspired Waste Material for Bioremediation of Pb2+ with Energy Generation through Microbial Fuel Cells. Chem. Eng. J., 128052

Yaqoob, A.A., Khatoon, A., Mohd Setapar, S.H., Umar, K., Parveen, T., Mohamad Ibrahim, M.N., Ahmad, A., Rafatullah, M., 2020c. Outlook on the Role of Microbial Fuel Cells in Remediation of Environmental Pollutants with Electricity Generation. Cataly. 10 (8), 819.

Yaqoob, A.A., Mohamad Ibrahim, M.N., Rafatullah, M., Chua, Y.S., Ahmad, A., Umar, K., 2020d. Recent Advances in Anodes for Microbial Fuel Cells: An Overview. Mater. 13 (9), 2078.

Yaqoob, A.A., Mohamad Ibrahim, M.N., Umar, K., Bhawani, S.A., Khan, A., Asiri, A.M., Khan, M.R., Azam, M., AlAmmari, A.M., 2021. Cellulose Derived Graphene/Polyaniline Nanocomposite Anode for Energy Generation and Bioremediation of Toxic Metals via Benthic Microbial Fuel Cells. Polym. 13 (1), 135.

Yaqoob, A.A., Parveen, T., Umar, K., Mohamad Ibrahim, M.N., 2020e. Role of nanomaterials in the treatment of wastewater: A review. Wat. 12 (2), 495.

Zaaba, N., Foo, K., Hashim, U., Tan, S., Liu, W.-W., Voon, C., 2017. Synthesis of graphene oxide using modified hummers method: solvent influence. Procedia Eng. 184, 469–477.

Zhang, L., Zhou, S., Zhuang, L., Li, W., Zhang, J., Lu, N., Deng, L., 2008. Microbial fuel cell based on Klebsiella pneumoniae biofilm. Electrochem. Commun. 10 (10), 1641–1643.

Zhang, Y., He, Q., Xia, L., Li, Y., Song, S., 2018. Algae cathode microbial fuel cells for cadmium removal with simultaneous electricity production using nickel foam/graphene electrode. Biochem. Eng. J. 138, 179–187.

Zhao, Y., Nakanishi, S., Watanabe, K., Hashimoto, K., 2011. Hydroxylated and aminated polyaniline nanowire networks for improving anode performance in microbial fuel cells. J. Biosci. Bioeng. 112 (1), 63–66.